On the micromechanism of inclusion driven ductile fracture and its implications on fracture toughness

Yu Liu[a], Xinzhu Zheng[a], Shmuel Osovski[b], Ankit Srivastava[a,*]

[a]*Department of Materials Science and Engineering, Texas A&M University, College Station, TX, USA*
[b]*Faculty of Mechanical Engineering, Technion - Israel Institute of Technology, Haifa, Israel*

Abstract

The objective is to identify the micromechanism(s) of ductile crack advance, and isolate the key microstructural and material parameters that affect these micromechanisms and fracture toughness of ductile structural materials. Three dimensional, finite element, finite deformation, small scale yielding calculations of mode I crack growth are carried out for ductile material matrix containing two populations of void nucleating particles using an elasto-viscoplastic constitutive framework for progressively cavitating solid. The larger particles or inclusions that result in void nucleation at an early stage are modeled discretely while smaller particles that require large strains to nucleate voids are homogeneously distributed. The size, spacing and volume fraction of inclusions introduce microstructure-based length-scales. In the calculations, ductile crack growth is computed and fracture toughness is characterized. Several features of crack growth behavior and dependence of fracture toughness on microstructural and material parameters observed in experiments, naturally emerge in our calculations. The extent to which the microstructural and material parameters affect the micromechanisms of ductile crack advance and, hence, the macroscopic fracture toughness of the material is discussed. The results presented provide guidelines for microstructural engineering to increase ductile fracture toughness, for example, the results show that for a material with small inclusions, increasing the mean inclusion spacing has a greater effect on fracture toughness than for a material with large inclusions.

Keywords: Fracture mechanism, Fracture toughness, Voids and inclusions, Finite elements, Ductile fracture

1. Introduction

The objective of this work is to correlate the macroscopic fracture toughness of heterogeneous ductile materials with the fracture mechanisms operating at the microscale. The focus is confined to ductile structural materials undergoing fracture due to nucleation, growth and coalescence of microscale voids (Tipper, 1949; Goods and Brown, 1979; Tvergaard, 1989;

*

Email address: `ankit.sri@tamu.edu` (Ankit Srivastava)

Benzerga and Leblond, 2010; Benzerga et al., 2016). The microstructure of such materials can be idealized as a ductile material matrix with randomly distributed inclusions or second phase particles, as is encountered in a variety of ferrous and aluminum alloys. The second phase particles in such materials are either added intentionally to the material's microstructure, for precipitation-hardening or dispersion-strengthening (Martin, 2012), or their formation is an unavoidable consequence of processing (Birat, 2016).

There is an important difference between the characterization of fracture in a deformation field that is more or less uniform and the characterization of fracture in a deformation field that is heterogeneous (Rice and Johnson, 1970; Rice, 1976; McMeeking, 1977; Aravas and McMeeking, 1985a; Needleman and Tvergaard, 1987; Gao et al., 1998; Tang et al., 2013; Srivastava et al., 2014). In the former, an unstructured continuum description of ductile fracture, in principle, can be based on material parameters such as strength and strain hardening exponent. On the other hand, in the latter, the macroscopic fracture toughness must involve characteristic length-scales associated with the material microstructure. This expected dependence of fracture toughness on material length-scales is consistent with the experimental results of ductile fracture due to nucleation, growth and coalescence of microscale voids in ductile structural materials (Edelson and Baldwin Jr, 1959; Krafft, 1964; Birkle et al., 1966; Spitzig, 1969; Hahn et al., 1972; Passoja and Hill, 1974; Green and Knott, 1976; Lautridou and Pineau, 1981; Garrison and Moody, 1987; Dubensky and Koss, 1987; Becker, 1987; Garrison et al., 1997; Benzerga et al., 1999; Jie et al., 2007; Garrison Jr and Wojcieszynski, 2009).

Several attempts have been made in the past to correlate material microstructural parameters such as volume fraction, size and spacing of the inclusions/voids with the macroscopic fracture toughness of the material. The mode I plane strain fracture toughness, K_{IC}, of several ductile materials has been shown to follow $K_{IC} = EN(2\pi L)^{\frac{1}{2}}$ (Krafft, 1964) or $K_{IC} \approx \sqrt{2\sigma_0 E\lambda}$ (Hahn and Rosenfield, 1975), where E is Young's modulus, N is the work hardening coefficient, σ_0 is the flow strength, L is the size of the process zone and λ is the spacing of the nearest void/inclusion from the initial crack tip. Often the process zone size has been hypothesized to correlate with the microstructural length-scale set by the pre-existing inclusions in the material (Birkle et al., 1966; Spitzig, 1969; Passoja and Hill, 1974). These suggest that the fracture toughness of the material predominantly depends on a single length-scale introduced by the mean (or extreme) spacing of the inclusions/voids. On the other hand, the fracture toughness of the material has been suggested to depend not only on the mean spacing but also on the size of the inclusions/voids. For example, the material's fracture toughness defined in terms of J_{IC} has been suggested to correlate with two microstructural length-scales as, $J_{IC} \propto \sigma_0 \left(2/{N_i}^{1/3}\right) \ln\left(r_c/r_0\right)$, where N_i is the number of inclusions per unit volume ($1/N_i^{1/3}$ is the mean inclusion spacing, l_0), r_0 is the initial size of the inclusions and r_c is the radius of the cavities at failure nucleated from these inclusions (Amar and Pineau, 1985). Dubensky and Koss (1987) carried out an experimental study to distinguish the influence of overall volume fraction, spacing and size of pre-existing voids/holes on material's ductility. Their experimental observation suggests that the spacing and size of the pre-existing voids has a larger effect on ductility compared to their volume fraction. The dominant effect of the spacing and/or size of the pre-existing inclusions/voids over their volume fraction on macroscopic fracture toughness has also been suggested by Benzerga et al. (1999); Van Stone and Psioda (1975); Shabrov and Needleman (2002).

The extent to which fracture toughness of a ductile material depends on the overall microstructural parameter i.e. volume fraction, or spacing and size of pre-existing voids has been associated with the micromechanisms of ductile crack advance. In general, two micromechanisms of ductile crack advance in a ductile material with preexisting distribution of voids have been proposed: crack advance by a void-by-void micromechanism and crack advance by multiple-void interaction (Tvergaard and Hutchinson, 2002; Kim et al., 2003; Pardoen and Hutchinson, 2003; Gao et al., 2005; Kim et al., 2007; Tvergaard, 2007; Tekoğlu et al., 2015). It has been suggested that for void-by-void micromechanism, $J_{IC}/(\sigma_0 l_0)$ or δ_c/l_0 (δ_c being the critical crack-tip opening displacement) depends on the initial void volume fraction whereas for multiple-void interaction micromechanism, $J_{IC}/(\sigma_0 l_0)$ or δ_c/l_0 does not depend on the initial void volume fraction. At the microscale, crack advance by the void-by-void micromechanism involves coalescence of the crack tip with the closest void (Rice and Johnson, 1970; Aravas and McMeeking, 1985a), whereas crack advance by multiple-void interaction involves simultaneous interaction of multiple voids ahead of the crack tip (Tvergaard and Hutchinson, 2002). The transition from the crack advance by the void-by-void micromechanism to multiple-void interaction has been shown to depend on the initial void volume fraction (Tvergaard and Hutchinson, 2002; Kim et al., 2003), wherein void-by-void micromechanism is operative at low initial void volume fraction and multiple-void interaction micromechanism is operative at high initial void volume fraction. However, Gao et al. (2005), suggested that other factors such as initial distribution of the voids can also affect the transition from void-by-void to multiple-void interaction micromechanism of ductile crack advance.

There is a distinct advantage of modeling discrete voids in a ductile matrix in the finite element calculations, e.g. Tvergaard and Hutchinson (2002); Gao et al. (2005), as this approach directly models the void growth behavior in the vicinity of a crack tip. However, it doesn't not naturally account for ductile crack advance. In addition, the class of ductile structural materials considered here, often contains a three-dimensional distribution of two populations of void nucleating particles: larger particles or inclusions (e.g. MnS inclusions in steels) that nucleate voids at relatively small strains and smaller particles (e.g. carbides in steels) that nucleate voids at larger strains. The voids nucleate either by debonding or cracking of the particles (Puttick, 1959; Rogers, 1960; Gurland and Plateau, 1963). Furthermore, the three-dimensional distribution of inclusions in a ductile matrix can promote crack meandering (Needleman and Tvergaard, 1987; Tang et al., 2013; Srivastava et al., 2014) and microcracking (Tinet et al., 2004; Srivastava et al., 2014) ahead of the initial crack tip well before the overall crack growth. Nevertheless, in Srivastava et al. (2014) it was shown that for a fixed initial inclusion size, $J_{IC}/(\sigma_0 l_0)$ depends on the inclusion volume fraction for small inclusion volume fractions whereas for larger inclusion volume fractions $J_{IC}/(\sigma_0 l_0)$ does not depend on the inclusion volume fraction. This raises several fundamental questions associated with inclusion driven ductile fracture: (i) Is the dependence of $J_{IC}/(\sigma_0 l_0)$ on inclusion volume fractions is due to the transition from void-by-void to multiple-void interaction micromechanism of ductile crack advance as has been suggested for ductile materials with pre-existing voids? (ii) How does the interlacing of two microstructural length-scales, inclusion spacing and size, affect the micromechanisms of ductile crack advance? (iii) How does the matrix material properties such as, strain hardening exponent, susceptibility to secondary void nucleation and energy dissipated in the growth of the nucleated voids prior to crack advance affect the micromechanisms of ductile crack advance?

To this end, finite element, finite deformation calculations are carried out using a constitutive framework for progressively cavitating ductile solid. The matrix material is modeled as an isotropic hardening elasto-viscoplastic solid together with two population of void nucleating particles. Larger particles or inclusions that result in void nucleation at an early stage are modeled discretely while smaller particles that require large strains to nucleate voids are homogeneously distributed. The size, spacing and volume fraction of inclusions introduce microstructure-based characteristic length-scales into the formulation. The calculations are carried out for small scale yielding conditions under remote Mode I loading. In the calculations, ductile crack growth are computed to the sufficient extent to be able to characterize the fracture toughness of the material in terms of J_{IC} using a procedure mimicking the ASTM:E1820-11 (2011). The extent to which the microstructural parameters such as volume fraction, size and spacing of the inclusions, and the properties of the matrix material affect the micromechanisms of ductile crack advance and hence the macroscopic fracture toughness of the material is discussed. The results presented also provide guidelines for microstructural engineering to increase fracture toughness.

2. Problem formulation and numerical method

2.1. Constitutive relation

The constitutive framework used here is the modified Gurson elastic-viscoplastic constitutive relation for a progressively cavitating solid (Gurson, 1975; Tvergaard and Needleman, 1984; Chu and Needleman, 1980) with the flow potential having the form

$$\Phi = \frac{\sigma_e^2}{\bar{\sigma}^2} + 2q_1 f^* \cosh\left(\frac{3q_2\sigma_h}{2\bar{\sigma}}\right) - 1 - (q_1 f^*)^2 = 0 \tag{1}$$

where $q_1 = 1.25$, $q_2 = 1.0$ are parameters introduced in Tvergaard (1981, 1982b), f^* is the effective void volume fraction, $\bar{\sigma}$ is the matrix flow strength, and

$$\sigma_e{}^2 = \frac{3}{2}\boldsymbol{\sigma}' : \boldsymbol{\sigma}' \quad , \quad \sigma_h = \frac{1}{3}\boldsymbol{\sigma} : \mathbf{I} \quad , \quad \boldsymbol{\sigma}' = \boldsymbol{\sigma} - \sigma_h \mathbf{I} \tag{2}$$

The function f^*, introduced in Tvergaard and Needleman (1984), is given by

$$f^* = \begin{cases} f, & f < f_c \\ f_c + (1/q_1 - f_c)(f - f_c)/(f_f - f_c), & f \geq f_c \end{cases} \tag{3}$$

where the values of $f_c = 0.12$ and $f_f = 0.25$ are used. Calculations are also carried out to explore the effect of the parameter f_c on the fracture toughness of the material for fixed microstructures.

The rate of deformation tensor is written as the sum of an elastic part, $\mathbf{d}^e = \mathbf{L}^{-1} : \hat{\boldsymbol{\sigma}}$, a viscoplastic part, $\mathbf{d}^p$, and a part due to thermal straining, $\mathbf{d}^\Theta = \alpha\dot{\Theta}\mathbf{I}$, so that

$$\mathbf{d} = \mathbf{L}^{-1} : \hat{\boldsymbol{\sigma}} + \alpha\dot{\Theta}\mathbf{I} + \mathbf{d}^p \tag{4}$$

Here, $\hat{\boldsymbol{\sigma}}$ is the Jaumann rate of Cauchy stress, Θ is the temperature, $\alpha = 1 \times 10^{-5}$/K is the thermal expansion coefficient and $\mathbf{L}$ is the tensor of isotropic elastic moduli. The plastic part of the strain rate, $\mathbf{d}^p$, is given by Pan et al. (1983)

$$\mathbf{d}^p = \left[\frac{(1-f)\bar{\sigma}\dot{\bar{\epsilon}}}{\boldsymbol{\sigma} : \frac{\partial\phi}{\partial\boldsymbol{\sigma}}}\right]\frac{\partial\phi}{\partial\boldsymbol{\sigma}} \tag{5}$$

The matrix plastic strain rate, $\dot{\bar{\epsilon}}$, is given by

$$\dot{\bar{\epsilon}} = \dot{\epsilon}_0\left[\frac{\bar{\sigma}}{g(\bar{\epsilon},\Theta)}\right]^{1/m} \quad , \quad g(\bar{\epsilon},\Theta) = \sigma_0 G(\Theta)\left[1 + \bar{\epsilon}/\epsilon_0\right]^N \tag{6}$$

with $\bar{\epsilon} = \int \dot{\bar{\epsilon}}dt$ and $\epsilon_0 = \sigma_0/E$. In the calculations the values of Young's modulus, $E =$ 70GPa, Poisson's ratio, $\nu = 0.3$, initial flow strength, $\sigma_0 = 300$MPa, ($\epsilon_0 = \sigma_0/E = 0.00429$), strain hardening exponent, $N = 0.1$, strain rate sensitivity exponent, $m = 0.01$, and reference strain rate, $\dot{\epsilon}_0 = 10^3\text{s}^{-1}$, are used. The value of $\dot{\epsilon}_0$ provides a reference strain rate so that for $\dot{\bar{\epsilon}} = \dot{\epsilon}_0$, $\bar{\sigma} = g$ in Eq. (6). The value of $\dot{\epsilon}_0 = 10^3\text{s}^{-1}$ is used here since it and other material parameters have the same values as employed in Srivastava et al. (2014); Osovski et al. (2015a); Srivastava et al. (2017). Parametric studies are also carried out to explore the effect of the matrix strain hardening exponent, N, on the fracture toughness of the material for fixed microstructures.

Adiabatic conditions are assumed so that

$$\rho c_p \frac{\partial\Theta}{\partial t} = \chi\boldsymbol{\sigma} : \mathbf{d}^p \tag{7}$$

with ρ being the current density of the material (the initial density, $\rho_0 = 7600\text{kg/m}^3$), $c_p = 465$J/(kg °K), $\chi = 0.9$, and the temperature-dependence of the flow strength, Eq. (6), is given by

$$G(\Theta) = 1 + b_G \exp(-c[\Theta_0 - 273])\left[\exp(-c[\Theta - \Theta_0]) - 1\right] \tag{8}$$

with $b_G = 0.1406$ and $c = 0.00793$/K. In Eq. (8), Θ and Θ_0 are in K and $\Theta_0 = 293$K. Also, the initial temperature is taken to be uniform and 293K.

The initial void volume fraction is taken to be zero and the evolution of the void volume fraction is governed by

$$\dot{f} = (1-f)\mathbf{d}^p : \mathbf{I} + \dot{f}_{nucl} \tag{9}$$

where the first term on the right hand side of Eq. (9) accounts for void growth and the second term accounts for void nucleation.

The constitutive framework employed in this work includes many of the hardening and softening mechanisms shown by ductile metallic materials. The values of the constitutive and material parameters used here follows the work of Srivastava et al. (2014). Most material parameters, such as elastic constants and reference yield stress, are representative of aluminum alloys. The initial density, however, is taken to be greater than that for aluminum to increase the stable time increment in the dynamic calculations.

2.2. Numerical implementation

A mode I small scale yielding boundary value problem is analyzed for a slice of material with an initial through thickness crack, as shown in Fig. 1. The slice of material analyzed has the dimensions $h_x \times h_y \times h_z$, where, $h_x = h_y = 0.4$m and $h_z/h_x = 0.0125$. The finite element mesh consists of $428,256$ twenty node brick elements giving $1,868,230$ nodes and $5,604,690$ degrees of freedom. Ten uniformly spaced elements are used through the thickness h_z. A uniform 208×64 in-plane ($x-y$ plane) mesh is used in a 0.02m $\times$ 0.006m region immediately in front of the initial crack front with in-plane elements of dimension 9.62×10^{-5}m by 9.38×10^{-5}m. The element dimension $e_x = 9.62 \times 10^{-5}$m serves as a normalization length. The initial crack front with an initial opening $b_0 = 1.95e_x$ lies along $(0,0,z)$ and the crack faces remain traction free. In the $x-y$ plane, velocity boundary conditions corresponding to linear isotropic mode I crack tip field are prescribed,

$$\dot{u}_x\left(R,\theta,z,t\right) = \frac{2\left(1+\nu\right)\dot{K}_I}{E}\sqrt{\frac{R}{2\pi}}\cos\frac{\theta}{2}\left(1-2\nu+\sin^2\frac{\theta}{2}\right) \tag{10}$$

$$\dot{u}_y\left(R,\theta,z,t\right) = \frac{2\left(1+\nu\right)\dot{K}_I}{E}\sqrt{\frac{R}{2\pi}}\sin\frac{\theta}{2}\left(2-2\nu-\cos^2\frac{\theta}{2}\right) \tag{11}$$

Here, $R^2 = x^2+y^2$ and $\theta = \tan^{-1}\left(y/x\right)$ for points on the boundary of the region analyzed, $\dot{K}_I$ is the prescribed rate of increase of the mode I stress intensity factor. Also, symmetry boundary conditions are imposed on $z = 0$, h_z planes. The value of $\dot{K}_I/\left(\dot{\epsilon}_0\sigma_0\sqrt{e_x}\right) = 1359.4$ is prescribed for it to be same as in Srivastava et al. (2014, 2017). The finite element calculations are based on the dynamic principle of virtual work using a finite deformation Lagrangian convected coordinate formulation. The calculations are based on the dynamic principle of virtual work for numerical convenience, hence to minimize the wave effects, initial velocity fields at $t = 0$ consistent with Eqs. (10) and (11) are prescribed throughout the region analyzed.

Eight point Gaussian integration is used in each twenty-node element for integrating the internal force contributions and twenty-seven point Gaussian integration is used for the element mass matrix. Lumped masses are used so that the mass matrix is diagonal. The discretized equations are integrated using the explicit Newmark β-method ($\beta = 0$) (Belytschko et al., 1976). The constitutive updating is based on the rate tangent modulus method proposed in Peirce et al. (1984), while material failure is implemented via the element vanish technique proposed in Tvergaard (1982a). When the value of the void volume fraction f at an integration point reaches $0.9f_f$, the value of f is kept fixed so that the material deforms with a very low flow strength. The entire element is taken to vanish when three of the eight integration points in the element have reached this stage.

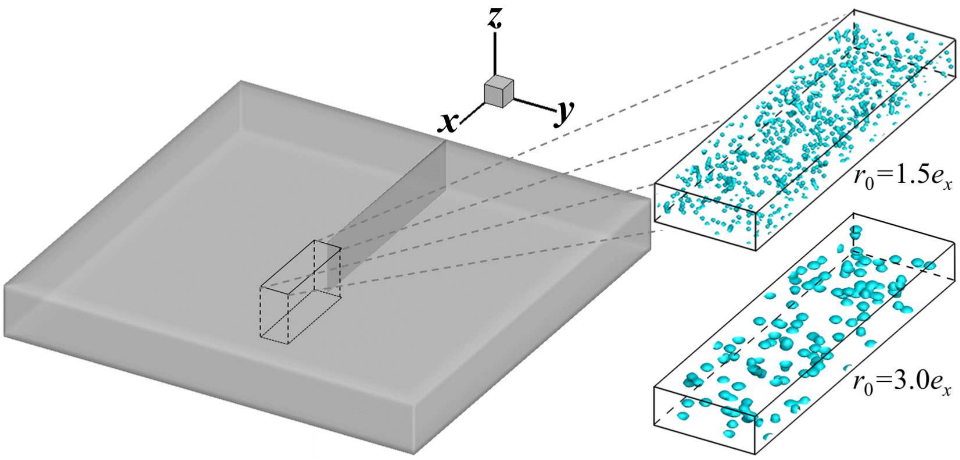

Figure 1: Sketch of the initially cracked block of material analyzed together with the magnified view of the three-dimensional random distributions of inclusions in front the initial crack. For the two distributions shown: (top right) radius of the inclusions, $r_0 = 1.5e_x$ and volume fraction, $n = 0.024$; and (bottom right) radius of the inclusions, $r_0 = 3.0e_x$ and volume fraction, $n = 0.024$. The parameter e_x is the normalization length parameter.

3. Microstructure generation

In the calculations the material microstructure is characterized by two populations of void nucleating particles: (i) uniformly distributed small particles that are modeled by plastic strain controlled void nucleation; and (ii) large particles or inclusions that are modeled as stress controlled nucleation sites. In each case, void nucleation is assumed to be described by a normal distribution following Chu and Needleman (1980).

For plastic strain nucleation

$$\dot{f}_{nucl} = k_\epsilon \dot{\bar{\epsilon}} \ , \ \ k_\epsilon = \frac{f_N}{s_N\sqrt{2\pi}} \exp\left[-\frac{1}{2}\left(\frac{\bar{\epsilon} - \epsilon_N}{s_N}\right)^2\right] \tag{12}$$

with $f_N = 0.04$, $\epsilon_N = 0.3$ and $s_N = 0.1$. Parametric studies are also carried out to explore the effect of the mean equivalent plastic strain to void nucleation in the matrix material, ϵ_N, on the fracture toughness for fixed microstructures.

For stress controlled nucleation

$$\dot{f}_{nucl} = k_\sigma \left[\dot{\bar{\sigma}} + \dot{\sigma}_h\right] \ , \ \ k_\sigma = \frac{f_N}{s_N\sqrt{2\pi}} \exp\left[-\frac{1}{2}\left(\frac{\bar{\sigma} + \sigma_h - \sigma_N}{s_N}\right)^2\right] \tag{13}$$

if $(\bar{\sigma}+\sigma_h) \geq (\bar{\sigma}+\sigma_h)_{max}$, where the maximum is taken over the previous mechanical history, and $\partial(\bar{\sigma}+\sigma_h)/\partial t > 0$. Otherwise, $k_\sigma = 0$. To generate the random distribution of inclusions (modeled discretely as stress controlled nucleation sites, Eq. (13)) within the uniform mesh region of volume, $V_u = 200e_x \times 60e_x \times 50e_x$, in front of the initial crack front, we first randomly generate predetermined number of inclusion, N_{incl}, centers (x_0, y_0, z_0) with the restriction that the center to center distance of two neighboring inclusions is at least twice the radius, r_0. The value of f_N in Eq. (13) at a material (Gaussian) point (x, y, z) in the initial undeformed configuration, is then assigned as,

$$f_N = \begin{cases} \bar{f}_N & \text{for } \sqrt{(x-x_0)^2 + (y-y_0)^2 + (z-z_0)^2} \leq r_0 \\ \\ 0 & \text{for } \sqrt{(x-x_0)^2 + (y-y_0)^2 + (z-z_0)^2} > r_0 \end{cases} \tag{14}$$

The values $\bar{f}_N = 0.04$, $s_N/\sigma_0 = 0.2$ and $\sigma_N/\sigma_0 = 1.5$ are used in the calculations. The inclusion volume fraction n, and the mean inclusion spacing l_0 are estimated as, $n = (N_{incl} \times 4\pi r_0^3/3)/V_u$ and $l_0 = (V_u/N_{incl})^{1/3}$, respectively. The inclusions introduce microstructure-based characteristic length-scales into the formulation, one associated with their spacing and the other with their size. Two random distributions of inclusions with $n = 0.024$, and $r_0 = 1.5e_x$ and $3.0e_x$ in the volume V_u, ahead of the initial crack front are shown in Fig. 1.

4. Results and discussion

The calculations are carried out for three radii, $r_0 = 1.5e_x$, $3.0e_x$ and $4.5e_x$ (where e_x is the normalization length parameter) of inclusions, and for a fixed r_0 the calculations are carried out for six inclusion volume fractions, $n = 0.012$, 0.024, 0.048, 0.071, 0.095 and 0.19. In addition, for a fixed r_0 and n, the calculations are carried out for five random distributions of inclusion centers i.e. five realizations of the same overall microstructure. Parametric studies are also carried out to explore the effect of the matrix material properties on the micromechanisms of ductile crack advance and fracture toughness of the material.

4.1. Crack growth resistance

Crack growth resistance $(J - R)$ curves, plots of J versus Δa, are extracted from all the calculations following the procedure adopted in Srivastava et al. (2014); Osovski et al. (2015a,b); Srivastava et al. (2017). The value of J is calculated from the applied value of K_I using the relation (Rice, 1968),

$$J = K_I^2 \frac{(1-\nu^2)}{E} \tag{15}$$

and the crack growth extension, Δa, is obtained by averaging the maximum projected length of the $f = 0.1$ contours through the thickness of the block of the material analyzed, Fig. 1.

The normalized $J - R$ curves for two inclusion radii, $r_0 = 1.5e_x$ and $4.5e_x$ and for each r_0, two inclusion volume fractions, $n = 0.024$ and 0.095 are shown in Fig. 2. For a fixed r_0 and n, the crack growth resistance curves are shown for three realizations of the same overall microstructure. In Fig. 2, the value of J is normalized by $\sigma_0 l_0$, while Δa is normalized by l_0. As seen in Fig. 2, for a fixed inclusion volume fraction, the level of the normalized $J - R$ curve is greater for the smaller inclusion radius, and for a fixed inclusion radius, the level of the normalized $J - R$ curve is greater for the smaller inclusion volume fraction. The variation in the $J - R$ curves between different realizations of the microstructure with a fixed r_0 and n, mainly stems from the initial stage of crack growth. The initiation of crack growth

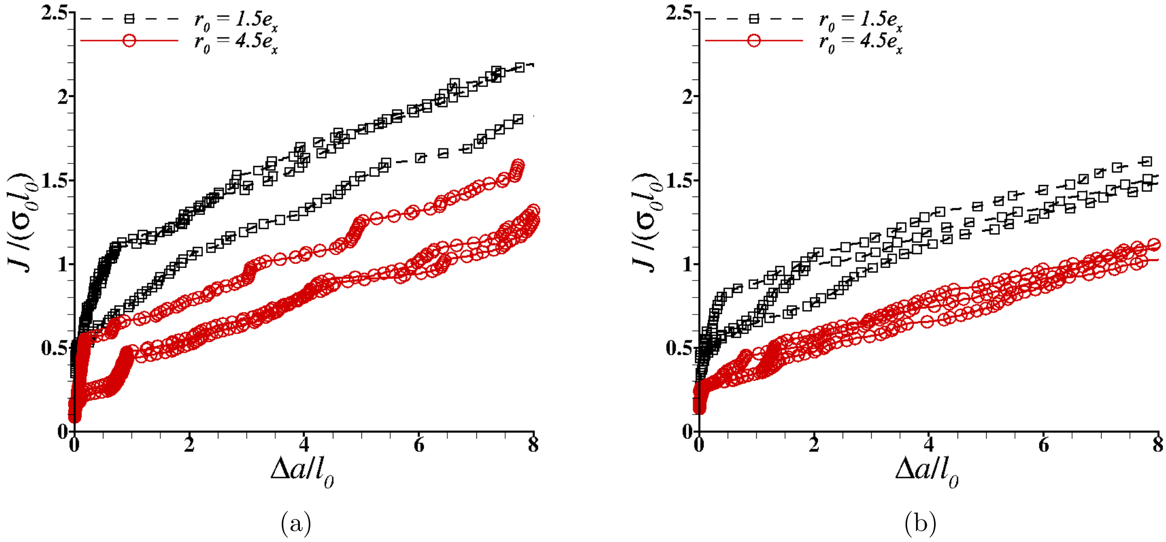

Figure 2: Applied normalized J, $J/(\sigma_0 l_0)$, versus normalized crack extension, $\Delta a/l_0$, curves for two inclusion radii, $r_0 = 1.5e_x$ and $4.5e_x$ with overall inclusion volume fractions, (a) $n = 0.024$ and (b) $n = 0.095$. For a fixed r_0 and n, results are shown for three random distributions of the inclusions.

depends on the interaction of the initial crack front with the nearest inclusions. Thus, for smaller inclusion volume fraction, Fig. 2a, the variation among the various realizations is greater than the larger inclusion volume fraction, Fig. 2b.

The fracture initiation toughness, J_{IC}, is computed based on a procedure mimicking the ASTM:E1820-11 (2011), where a power law of the form $J = A(\Delta a)^B$ is fit to the portion of the $J-R$ curve in between two exclusion lines, $J = 2\sigma_0(\Delta a - 1.5e_x)$ and $J = 2\sigma_0(\Delta a - 5e_x)$. The value of J_{IC} is then defined as the intersection of the curve $J = A(\Delta a)^B$ and the line $J = 2\sigma_0(\Delta a - 2e_x)$. The variation of normalized fracture toughness, $J_{IC}/(\sigma_0 l_0)$, with inclusion volume fraction, n, for three inclusion radii are shown in Fig. 3. The error bars in Fig. 3 show the standard errors (standard deviation divided by the square root of the number of realizations) for realizations of inclusion distributions having the same value of r_0 and n. The dash-dot lines in Fig. 3 for $r_0 = 1.5e_x$ show a fit to $J_{IC}/(\sigma_0 l_0) = C_1 n^{C_2} + C_3 r_0 + C_4$, and for $r_0 = 3.0e_x$ and $4.5e_x$ show a fit to $J_{IC}/(\sigma_0 l_0) = C_3 r_0 + C_4$, where $C_1 = 0.01$, $C_2 = -0.8$, $C_3 = -0.1e_x$ and $C_4 = 0.85$. The results presented in Fig. 3 show that for a fixed set of material parameters, for the smallest inclusion radius considered here, $r_0 = 1.5e_x$, the value of $J_{IC}/(\sigma_0 l_0)$ decreases rapidly with increasing n for $n \leq 0.071$ and then tends to saturate. But for the two larger inclusion radii, $r_0 = 3.0e_x$ and $4.5e_x$, the value of $J_{IC}/(\sigma_0 l_0)$ is rather independent of n, for the range of n considered.

In all the previous works, on the interaction of: (i) explicitly modeled two-dimensional distribution of (cylindrical plane-strain) voids or three-dimensional distribution of (spherical) voids with a blunting crack tip (Rice and Johnson, 1970; McMeeking, 1977; Aravas and McMeeking, 1985a,b; Hom and McMeeking, 1989; Kim et al., 2003), or (ii) explicitly

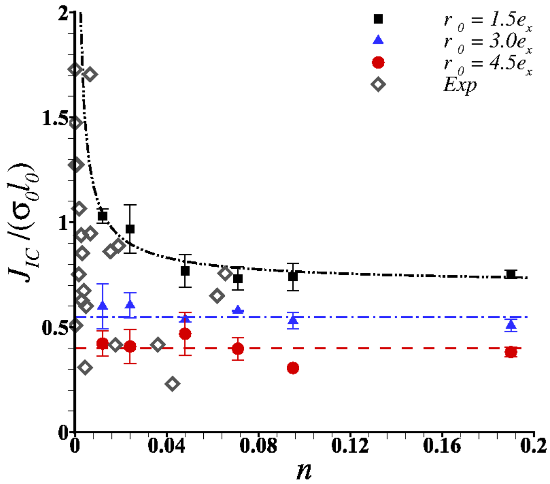

Figure 3: Variation of normalized fracture toughness, J_{IC}, $J_{IC}/(\sigma_0 l_0)$, with inclusion volume fraction, n, for three inclusion radii, $r_0 = 1.5e_x$, $3.0e_x$ and $4.5e_x$. The lines are the fitted curves and the data labeled, *Exp*, are the experimental results summarized by McMeeking (1977). In the experiments, the crack-tip opening displacement at initiation of crack growth, δ_c, were measured that are converted to J_{IC}, following the relation, $J_{IC} = m\sigma_0\delta_c$ (Shih, 1981), where $m = 1$.

modeled two-dimensional or three-dimensional distribution of (void nucleating) inclusions with a growing crack tip (Needleman and Tvergaard, 1987; Srivastava et al., 2014), the focus was confined on correlating macroscopic fracture initiation toughness defined using δ_c/l_0 or $J_{IC}/(\sigma_0 l_0)$ with the microstructural parameter defined either using the ratio of mean void/inclusion spacing and size, $l_0/2r_0$ or void/inclusion volume fraction, n (where $n \propto (r_0/l_0)^3$). These calculations predict that for a fixed set of material parameters, the value of δ_c/l_0 or $J_{IC}/(\sigma_0 l_0)$ is uniquely related to $l_0/2r_0$ or n, and the value of δ_c/l_0 or $J_{IC}/(\sigma_0 l_0)$ initially increases rapidly with increasing $l_0/2r_0$ (decreasing n) and then tends to saturate. These calculations did not predict the variation in the values of $J_{IC}/(\sigma_0 l_0)$ for a fixed n. Our results, Fig. 3, show that for high inclusion volume fraction $J_{IC}/(\sigma_0 l_0)$ depends on the inclusion size whereas for low inclusion volume fraction $J_{IC}/(\sigma_0 l_0)$ depends on both the inclusion size and the inclusion volume fraction. The normalized experimental results plotted in Fig. 3 follows the same trend even though the experimental results are for a wide variety of engineering metals and alloys. The experimental results shown in Fig. 3 were summarized by McMeeking (1977), further details of the experimental results can be found in the references given in McMeeking (1977). These experimental results were also used for comparison purposes in Aravas and McMeeking (1985a,b); Needleman and Tvergaard (1987); Tvergaard and Hutchinson (2002).

4.2. Micromechanism of ductile crack advance

Whether or not $J_{IC}/(\sigma_0 l_0)$ or δ_c/l_0, depends on the overall microstructural parameter i.e. volume fraction of the initial voids or the inclusions, n, has been associated with the void-

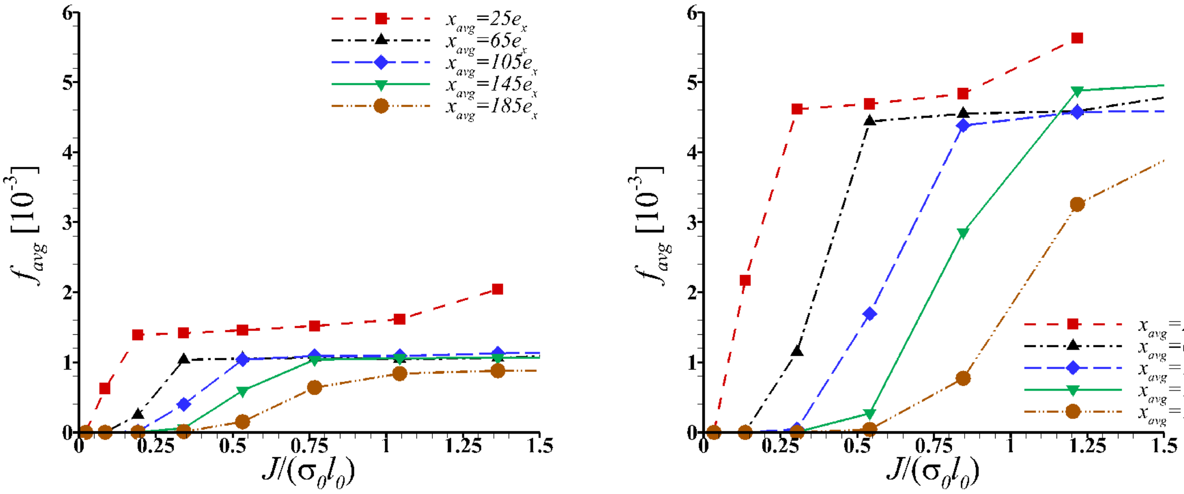

(a) (b)

Figure 4: Evolution of average porosity, f_{avg}, in the bins located at distances x_{avg} directly ahead of the initial crack tip with applied normalized J, $J/(\sigma_0 l_0)$, for random distributions of inclusions of radius $r_0 = 1.5e_x$ and overall inclusion volume fractions, (a) $n = 0.024$ and (b) $n = 0.095$.

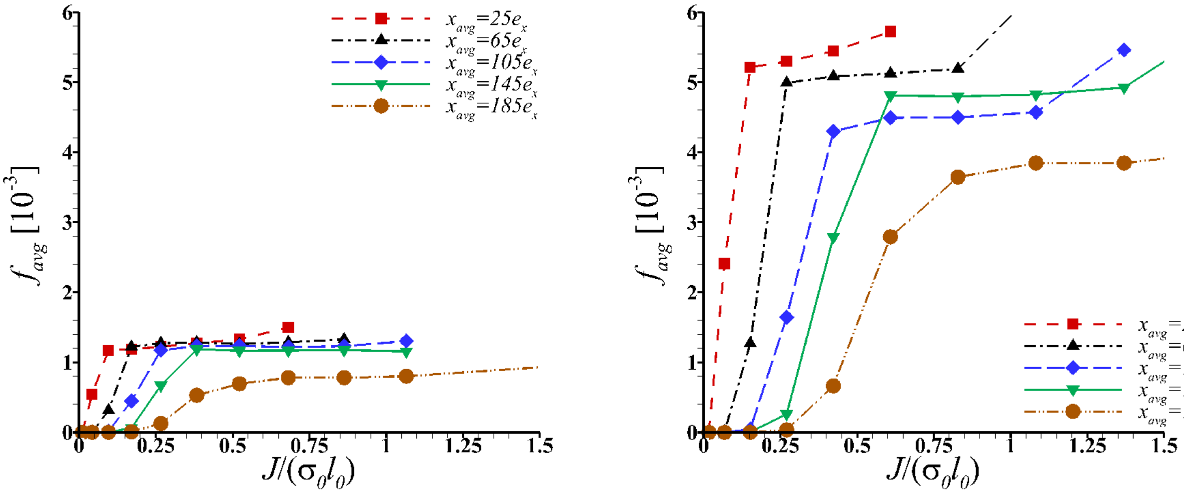

(a) (b)

Figure 5: Evolution of average porosity, f_{avg}, in the bins located at distances x_{avg} directly ahead of the initial crack tip with applied normalized J, $J/(\sigma_0 l_0)$, for random distributions of inclusions of radius $r_0 = 3.0e_x$ and overall inclusion volume fractions, (a) $n = 0.024$ and (b) $n = 0.095$.

by-void or multiple-void interaction micromechanism of ductile crack advance, respectively (Tvergaard and Hutchinson, 2002; Kim et al., 2003; Srivastava et al., 2014). Following this, from the variation of $J_{IC}/(\sigma_0 l_0)$ with n in Fig. 3, for $r_0 = 1.5e_x$ and $n \leq 0.071$

the ductile crack advance can be associated with void-by-void micromechanism whereas for all other cases ductile crack advance can be associated with multiple-void interaction micromechanism. Tvergaard and Hutchinson (2002) carried out simple but detailed analyses of growth of a row of explicitly modeled two-dimensional (cylindrical plane-strain) voids ahead of a blunting crack tip and showed that for low initial void volume fraction, voids grow one-by-one (starting from the void closest to the crack tip), whereas for high initial void volume fraction, many-voids ahead of the crack tip grow simultaneously. However, unlike the scenario modeled in Tvergaard and Hutchinson (2002), the material microstructure modeled here has randomly distributed inclusions in a ductile material matrix. This prohibits us from applying the similar analysis as in Tvergaard and Hutchinson (2002) to identify or distinguish between the void-by-void and multiple-void interaction micromechanisms of ductile crack advance. Thus, we analyze the evolution of average porosity with the applied J in thin slices of the inclusion containing material volume ahead of the initial crack tip.

To this end, we divide the uniform mesh region that contains three dimensional random distribution of inclusions (see Fig. 1) in to 20 cuboidal bins of height $60e_x$, thickness $50e_x$, and width $10e_x$. The average porosity, f_{avg}, in a bin is then estimated as,

$$f_{avg} = \sum_i \frac{V_i f_i}{V_{bin}} \tag{16}$$

where, i is the number of elements in the bin, V_i is the volume of element i, f_i is the average value of porosity in the element i and V_{bin} is the volume of the bin. The value of f_{avg} in a bin is estimated until the bin is crack free. The evolution of f_{avg} in the bins located at an average distance, x_{avg}, from the initial crack tip with applied normalized J, $J/\left(\sigma_0 l_0\right)$, for two inclusion volume fractions, $n = 0.024$ and 0.095, with $r_0 = 1.5e_x$ are shown in Fig. 4 and with $r_0 = 3e_x$ are shown in Fig. 5.

Based on the observations of Tvergaard and Hutchinson (2002), it would be expected that for $r_0 = 1.5e_x$ and $n = 0.024$, Fig. 4, the value of f_{avg} in the bins should evolve one-by-one (starting from the bin closest to the crack tip) and for all other cases shown in Figs. 4b, 5a and 5b, f_{avg} in many-bins ahead of the crack tip should evolve simultaneously with increasing $J/\left(\sigma_0 l_0\right)$. However, as shown in Figs. 4 and 5, for all the cases the value of $J/\left(\sigma_0 l_0\right)$ at which f_{avg} starts to evolve in a bin increases with increasing distance of the bin from the initial crack tip, suggesting f_{avg} in the bins evolve one-by-one. Also, for a given bin, the value of f_{avg} for all the cases initially increases rapidly with increasing $J/\left(\sigma_0 l_0\right)$ and then tends to increase rather slowly. There is, however, a clear difference between, Figs. 4a and 5a, and Figs. 4b and 5b, that suggests that the level of the f_{avg} versus $J/\left(\sigma_0 l_0\right)$ curve only depends on the inclusion volume fraction, n. The absence of a clear signature suggesting void-by-void or multiple-void interaction micromechanism of ductile crack advance in our analyses presented in Figs. 4 and 5, is likely due to the fact that the material microstructure in this work is characterized by randomly distributed inclusions in three-dimensional space for which the crack path is not fixed a priori.

The initial rapid increase in f_{avg} in a bin with increasing $J/\left(\sigma_0 l_0\right)$ seen in Figs. 4 and 5 arises from the stress controlled void nucleation at inclusions. In Fig. 6, isosurfaces of the

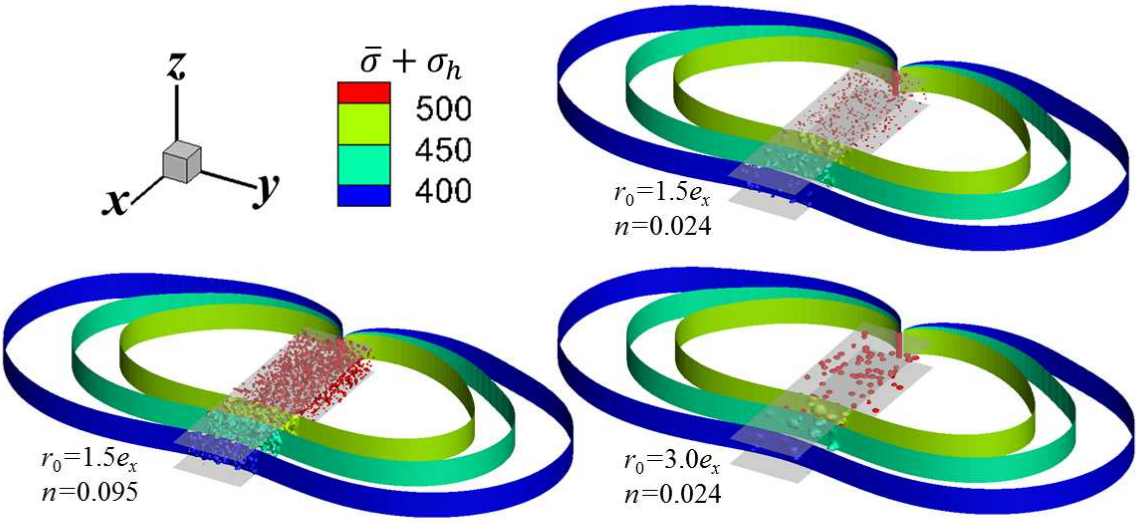

(a)

Figure 6: Isosurface plot of matrix flow strength, $\bar{\sigma}$, plus hydrostatic stress, σ_h, ahead of the initial crack tip together with active inclusions (inclusions that have already nucleated voids) at an applied normalized J, $J/(\sigma_0 l_0)$. The parameter $(\bar{\sigma} + \sigma_h)$ dictates the stress controlled nucleation of voids at the inclusion sites. For inclusions of radius $r_0 = 1.5e_x$ and overall inclusion volume fraction $n = 0.024$, $J/(\sigma_0 l_0) \approx 0.53$; for $r_0 = 1.5e_x$ and $n = 0.095$, $J/(\sigma_0 l_0) \approx 0.85$; and for $r_0 = 3.0e_x$ and $n = 0.024$, $J/(\sigma_0 l_0) \approx 0.27$.

matrix flow strength, $\bar{\sigma}$, plus the hydrostatic stress, σ_h, are plotted together with the active inclusions (inclusions that have already nucleated voids) for $r_0 = 1.5e_x$ with $n = 0.024$ and 0.095, and for $r_0 = 3.0e_x$ with $n = 0.024$. The parameter $\bar{\sigma} + \sigma_h$ is the driving force for void nucleation at the inclusions following the nucleation criteria in Eq. 13. For all the cases, the $\bar{\sigma} + \sigma_h$ isosurfaces in Fig. 6 are plotted at values of applied $J/(\sigma_0 l_0)$ that are less than the values of respective $J_{IC}/(\sigma_0 l_0)$. As seen in Fig. 6, at a fixed value of applied $J/(\sigma_0 l_0)$, the region ahead of the crack tip in which the inclusions are already active depends on the extent of $\bar{\sigma} + \sigma_h$ contours. Thus, for all the cases, f_{avg} in the bins due to void nucleation evolves one-by-one as seen in Figs. 4 and 5. The calculations also show that once the inclusions have nucleated voids in a bin, only few voids within a bin are found to grow significantly. Crack advance then occurs by linking up the crack tip with the growing voids in the bin via strain induced void nucleation and growth in the matrix, as also seen in experiments (Cox and Low, 1974). This results in very little void growth off the crack plane as has been observed experimentally for a variety of ductile materials (Ghahremaninezhad and Ravi-Chandar, 2012a,b). This also explains why, once all the inclusions in a bin have been activated there is a very little increase in f_{avg} in that bin and the level of the $J/(\sigma_0 l_0)$ versus f_{avg} curve predominantly depend on the value of n. We note that, no inclusion size effect on void nucleation is modeled here but in line with experimental observations, for example Van Stone and Psioda (1975); Garrison Jr and Wojcieszynski (2009), an increase in J_{IC} with decreasing inclusion size for the same l_0 naturally emerges in our calculations.

The variation of $J_{IC}/(\sigma_0 l_0)$ with n in Fig. 3, clearly suggest that the micromechanism of

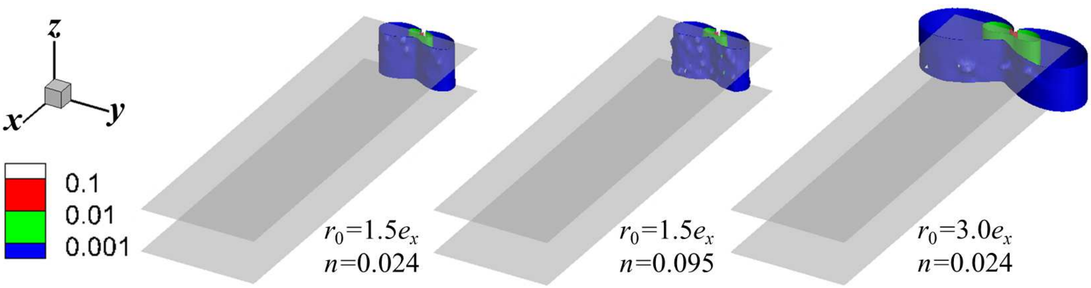

Figure 7: Isosurface plots of equivalent plastic strain ahead of the initial crack tip for random distributions of inclusions at an applied normalized J, $J/(\sigma_0 l_0)$. For inclusions of radius $r_0 = 1.5e_x$ and overall inclusion volume fraction $n = 0.024$, $J/(\sigma_0 l_0) \approx 0.09$; for $r_0 = 1.5e_x$ and $n = 0.095$, $J/(\sigma_0 l_0) \approx 0.14$; and for $r_0 = 3.0e_x$ and $n = 0.024$, $J/(\sigma_0 l_0) \approx 0.1$.

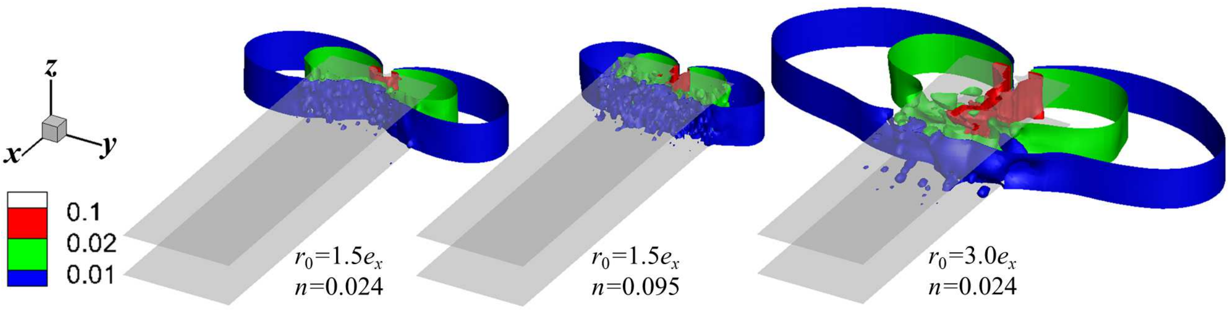

Figure 8: Isosurface plots of equivalent plastic strain ahead of the initial crack tip for random distributions of inclusions at an applied normalized J, $J/(\sigma_0 l_0)$. For inclusions of radius $r_0 = 1.5e_x$ and overall inclusion volume fraction $n = 0.024$, $J/(\sigma_0 l_0) \approx 1.04$; for $r_0 = 1.5e_x$ and $n = 0.095$, $J/(\sigma_0 l_0) \approx 1.22$; and for $r_0 = 3.0e_x$ and $n = 0.024$, $J/(\sigma_0 l_0) \approx 1.07$.

ductile crack advance for $r_0 = 1.5e_x$ and $n \leq 0.071$ differs from all other cases considered, even though it is not possible to identify these micromechanisms using analyses analogous to Tvergaard and Hutchinson (2002), Figs. 4 and 5. To further explore the micromechanisms of ductile crack advance, we plot the isosurfaces of equivalent plastic strain ahead of the initial crack tip for $r_0 = 1.5e_x$ with $n = 0.024$ and 0.095, and for $r_0 = 3.0e_x$ with $n = 0.024$ at two values of applied $J/(\sigma_0 l_0)$ in Figs. 7 and 8, respectively. In Fig. 7, the isosurfaces of equivalent plastic strain are plotted at values of applied $J/(\sigma_0 l_0)$ that are much less than the corresponding values of $J_{IC}/(\sigma_0 l_0)$ whereas in Fig. 8 the isosurfaces of equivalent plastic strain are plotted at values of applied $J/(\sigma_0 l_0)$ that are comparable to the corresponding values of $J_{IC}/(\sigma_0 l_0)$. As shown in Fig. 7, during the early stages of deformation the overall equivalent plastic strain distribution follows the expected pattern for plane strain Mode I loading with local perturbations due to stress controlled void nucleation at the inclusions. Following crack growth initiation for $r_0 = 1.5e_x$ with 0.095 and for $r_0 = 3.0e_x$ with $n = 0.024$, Fig. 8, plastic strain concentrates in a band. This shows that compared to the stress based void nucleation at inclusions, Fig. 6, the growth of nucleated voids and the plastic strain controlled secondary void nucleation in the material matrix are more sensitive to inclusion distribution. This is in line with the past experimental observations that have suggested that in ductile materials with increasing inclusions size or volume fraction final fracture occurs by microscopic plastic strain localization and secondary void nucleation between large voids (Rogers, 1960; Cox and Low, 1974; Hahn and Rosenfield, 1975; Stone et al., 1985).

The overall mechanism of ductile crack advance for all the cases considered is same in a way that following the stress based void nucleation at the inclusions, it involves growth of a limited number of nucleated voids and coalescence of these voids via plastic strain controlled secondary void nucleation in the material matrix. Nevertheless, our results show that there is an increase in the propensity of plastic strain localization with increasing inclusion volume fraction and/or size. This subtle change in the micromechanism of ductile crack advance results in the difference on the dependence of macroscopic fracture toughness on the material microstructure. So that for relatively low inclusion volume fraction and small inclusion size the normalized fracture toughness $J_{IC}/(\sigma_0 l_0)$ depends on both the inclusion size and the overall microstructural parameter i.e. inclusion volume fraction while for high inclusion volume fraction and large inclusion size $J_{IC}/(\sigma_0 l_0)$ depends only on the inclusion size. Furthermore, these results provide important guidelines for microstructural engineering to increase ductile fracture toughness, for example, the results show that for a material with small inclusions, increasing the mean inclusion spacing has a greater effect on fracture toughness than for a material with large inclusions.

4.3. Influence of matrix material properties

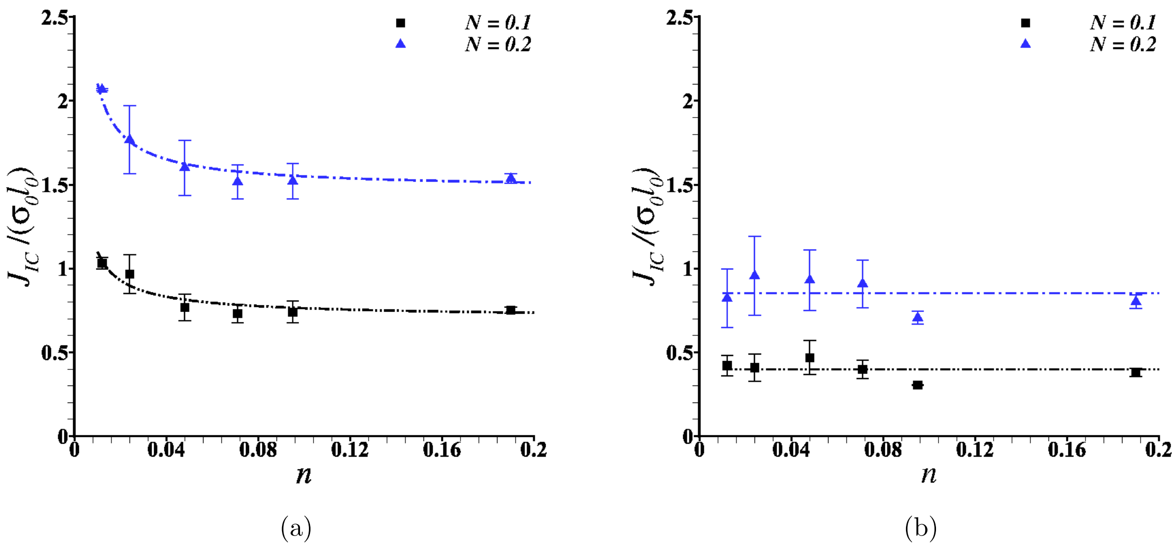

Figure 9: The effect of strain hardening exponent, N, on the variation of normalized fracture toughness, J_{IC}, $J_{IC}/(\sigma_0 l_0)$, with inclusion volume fraction, n, for inclusion radii, (a) $r_0 = 1.5e_x$ and (b) $r_0 = 4.5e_x$.

In this section we present the influence of key matrix material parameters on the micromechanisms of ductile crack advance and macroscopic fracture toughness of the material.

The matrix material parameters that are considered, are the matrix strain hardening exponent, N in Eq. (6), the mean equivalent plastic strain to void nucleation in the matrix, ϵ_N in Eq. (12), and the critical void volume fraction to void coalescence, f_c in Eq. (3).

The effect of the matrix strain hardening exponent, N, on the variation of normalized fracture toughness, $J_{IC}/(\sigma_0 l_0)$, with inclusion volume fraction, n, for inclusion radii, $r_0 = 1.5e_x$ and $4.5e_x$, are shown in Fig. 9. As shown in the figure, decreasing the value of N results in a decrease in the value of $J_{IC}/(\sigma_0 l_0)$ for all values of r_0 and n considered, with the effect of N being more pronounced for $r_0 = 1.5e_x$ than for $r_0 = 4.5e_x$. For the smallest inclusion radius, $r_0 = 1.5e_x$, the value of $J_{IC}/(\sigma_0 l_0)$ initially decreases with increasing n and then tends to saturate, whereas for $r_0 = 4.5e_x$ the value of $J_{IC}/(\sigma_0 l_0)$ is independent of the value of n for both the values of $N = 0.1$ and 0.2. The dashed-dot lines in Fig. 9a show a fit to $J_{IC}/(\sigma_0 l_0) = C_1 n^{C_2} + C_3$ and in Fig. 9b show a fit to $J_{IC}/(\sigma_0 l_0) = C_4$. In Fig. 9a, for $r_0 = 1.5e_x$, $C_1 = 0.01$ for both $N = 0.1$ and 0.2, for $N = 0.1$, $C_2 = -0.8$ and $C_3 = 0.7$, and for $N = 0.2$, $C_2 = -0.9$ and $C_3 = 1.47$. In Fig. 9b, for $r_0 = 4.5e_x$, $C_4 \approx 0.4$ and 0.9 for $N = 0.1$ and 0.2, respectively. The values of the fitting parameter C_2 for $N = 0.1$ and 0.2 for $r_0 = 1.5e_x$ shows that the dependence of $J_{IC}/(\sigma_0 l_0)$ on n decreases with decreasing strain hardening exponent. The decrease in the dependence of $J_{IC}/(\sigma_0 l_0)$ on n with decreasing N observed in our calculations is consistent with experimental observations (Bourcier et al., 1986). Bourcier et al. (1986) analyzed the influence of initial porosity on the ductility of commercial pure (CP) titanium (Ti) and Ti-6Al-4V alloy. They showed that the dependence of ductility on the initial volume fraction of porosity is greater for CP Ti for which $N \approx 0.19$ than the Ti-6Al-4V alloy for which $N \approx 0.08$.

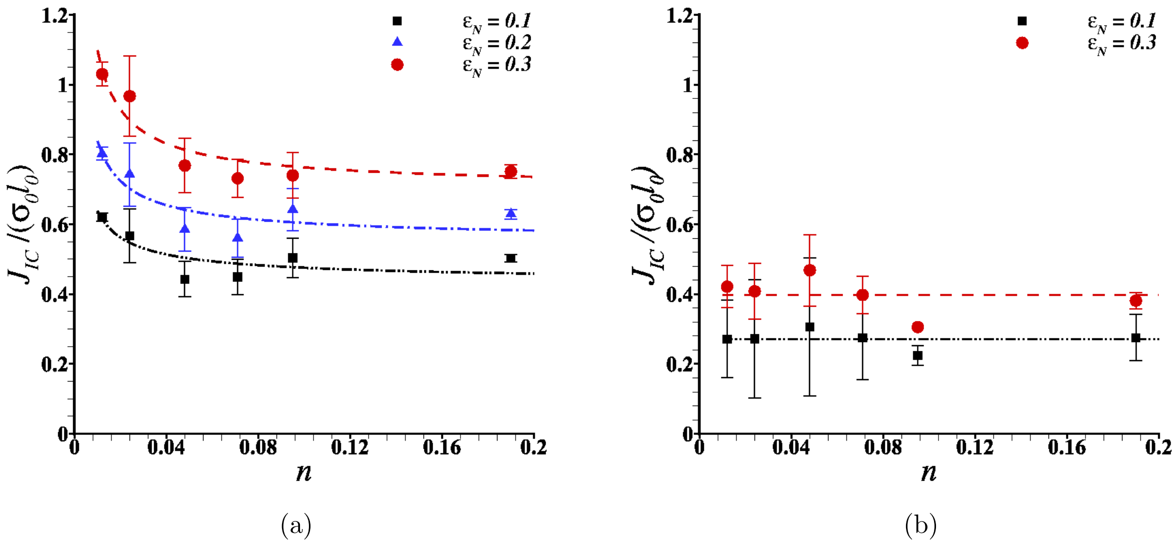

Figure 10: The effect of mean equivalent plastic strain to void nucleation in the matrix material, ϵ_N, on the variation of normalized fracture toughness, J_{IC}, $J_{IC}/(\sigma_0 l_0)$, with inclusion volume fraction, n, for inclusion radii, (a) $r_0 = 1.5e_x$ and (b) $r_0 = 4.5e_x$.

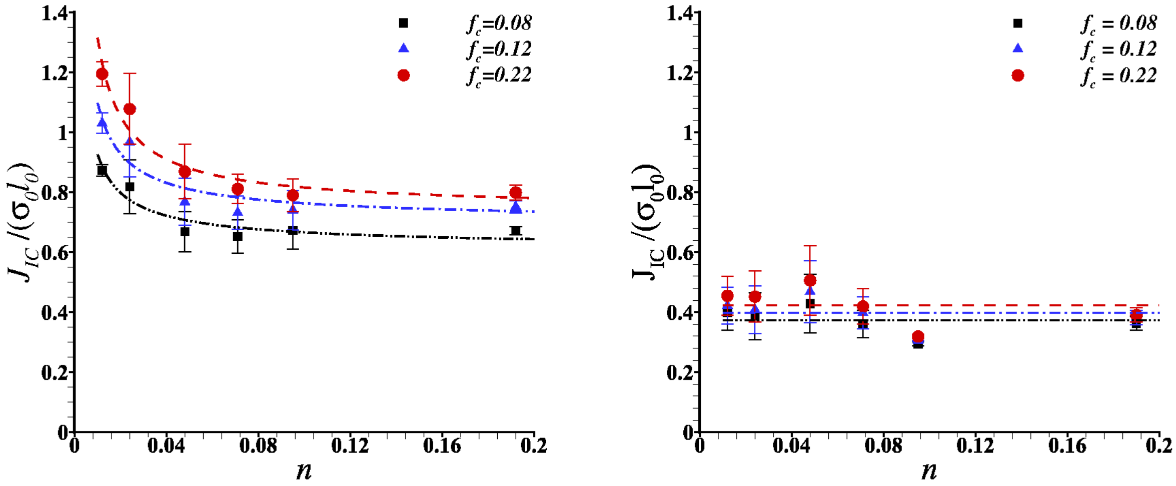

(a) (b)

Figure 11: The effect of critical volume fraction to void coalescence, f_c, on the variation of normalized fracture toughness, J_{IC}, $J_{IC}/\left(\sigma_0 l_0\right)$, with inclusion volume fraction, n, for inclusion radii, (a) $r_0 = 1.5e_x$ and (b) $r_0 = 4.5e_x$.

Next, we focus on the effect of mean equivalent plastic strain to void nucleation, ϵ_N, on the variation of $J_{IC}/\left(\sigma_0 l_0\right)$ with n and r_0, Fig. 10. The parameter ϵ_N dictates the secondary void nucleation in the material matrix. As shown in the figure, decreasing the value of ϵ_N results in a decrease in the value of $J_{IC}/\left(\sigma_0 l_0\right)$ for all values of r_0 and n considered. A decrease in fracture toughness of the material with increasing susceptibility to secondary void nucleation is consistent with previous works (Kim et al., 2003; Gall et al., 2000; Hannard et al., 2018). Similar to the effect of N, here as well, Fig. 10, the effect of ϵ_N is more pronounced for $r_0 = 1.5e_x$ than for $r_0 = 4.5e_x$, and for $r_0 = 1.5e_x$ the value of $J_{IC}/\left(\sigma_0 l_0\right)$ initially decreases with increasing n and then tends to saturate whereas for $r_0 = 4.5e_x$ the value of $J_{IC}/\left(\sigma_0 l_0\right)$ is independent of the value of n for all the values of ϵ_N considered. The dashed-dot lines in Fig. 10a show a fit to $J_{IC}/(\sigma_0 l_0) = C_1 n^{C_2} + C_3$ and in Fig. 10b show a fit to $J_{IC}/(\sigma_0 l_0) = C_4$. In Fig. 10a, for $r_0 = 1.5e_x$, $C_1 = 0.01$ for both $\epsilon_N = 0.1$ and 0.3, for $\epsilon_N = 0.1$, $C_2 = -0.66$ and $C_3 = 0.43$, and for $\epsilon_N = 0.3$, $C_2 = -0.8$ and $C_3 = 0.7$. In Fig. 10b, for $r_0 = 4.5e_x$, $C_4 \approx 0.3$ and 0.4 for $\epsilon_N = 0.1$ and 0.3, respectively. The values of the fitting parameter C_2 for $\epsilon_N = 0.1$ and 0.3 for $r_0 = 1.5e_x$ shows that the dependence of $J_{IC}/\left(\sigma_0 l_0\right)$ on n decreases with decrease in the value of ϵ_N or increasing susceptibility to secondary void nucleation.

Figure 11 shows the effect of the critical void volume fraction to void coalescence, f_c, on the variation of $J_{IC}/\left(\sigma_0 l_0\right)$ with n and r_0. The parameter f_c dictates the energy dissipated in the growth of the nucleated voids prior to crack advance. As shown in the figure, decreasing f_c results in a decrease in the value of $J_{IC}/\left(\sigma_0 l_0\right)$ for all values of r_0 and n considered. The effect of f_c on fracture toughness that emerges in our calculations is consistent with the experimentally observed correlation between the radius of the cavities at failure and the fracture toughness of the material (Amar and Pineau, 1985). Also, similar to the results shown in Figs. 9 and 10, here as well, Fig. 11, the effect of f_c is more pronounced for $r_0 = 1.5e_x$ than for $r_0 = 4.5e_x$, and for $r_0 = 1.5e_x$ the value of $J_{IC}/(\sigma_0 l_0)$ initially decreases with increasing n and then tends to saturate whereas for $r_0 = 4.5e_x$ the value of $J_{IC}/(\sigma_0 l_0)$ is independent of the value of n for all the values of f_c considered. The dashed-dot lines in Fig. 11a show a fit to $J_{IC}/(\sigma_0 l_0) = C_1 n^{C_2} + C_3$ and in Fig. 11b show a fit to $J_{IC}/(\sigma_0 l_0) = C_4$. In Fig. 11a, for $r_0 = 1.5e_x$, $C_1 = 0.01$ for both $f_c = 0.08$ and 0.22, for $f_c = 0.08$, $C_2 = -0.75$ and $C_3 = 0.61$, and for $f_c = 0.22$, $C_2 = -0.88$ and $C_3 = 0.74$. In Fig. 11b, for $r_0 = 4.5e_x$, $C_4 \approx 0.37$ and 0.42 for $f_c = 0.08$ and 0.22, respectively. The values of the fitting parameter C_2 for $f_c = 0.08$ and 0.22 for $r_0 = 1.5e_x$ shows that the dependence of $J_{IC}/(\sigma_0 l_0)$ on n decreases with decreasing value of the critical void volume fraction to void coalescence, f_c.

To summarize, the ductile fracture toughness of the material decreases with, decreasing strain hardening exponent of the matrix material (decreasing N), increasing susceptibility to secondary void nucleation in the matrix material (decreasing ϵ_N) and decreasing energy dissipation in the growth of the nucleated voids prior to crack advance (decreasing f_c). Furthermore, for the range of the values of N, ϵ_N and f_c considered, (i) the effect of these material parameters on fracture toughness is more pronounced for small inclusions than for large inclusions, and (ii) for small inclusions, the dependence of $J_{IC}/(\sigma_0 l_0)$ on inclusion volume fraction, n, decreases with decrease in the value of these material parameters, whereas for large inclusions the value of $J_{IC}/(\sigma_0 l_0)$ is always independent of the value of n. These observations are consistent with the discussion of micromechanisms of ductile crack advance presented in Section 4.2. As discussed in Section 4.2, the propensity of plastic strain localization increases with increasing inclusion size. Thus, for material microstructures with large inclusions, the damage induced softening due to inclusions is sufficient to cause plastic strain localization and decreasing the strain hardening exponent, increasing the susceptibility to secondary void nucleation or decreasing the energy dissipated in void growth just accelerates the localization process to various extents. Also, the dependence of $J_{IC}/(\sigma_0 l_0)$ on inclusion volume fraction decreases with increasing propensity of plastic strain localization. For material microstructures with small inclusions, the damage induced softening due to inclusions is not sufficient to cause plastic strain localization but a decrease in the strain hardening exponent, increase in the susceptibility to secondary void nucleation or decrease in the energy dissipated in void growth increases the propensity of plastic strain localization.

5. Concluding remarks

We have carried out finite element finite deformation calculations to correlate the macroscopic fracture toughness with the fracture mechanisms operating at the microscale for ductile material matrix with three-dimensional distribution of inclusions. While we have not aimed at modeling any particular real material, several features of crack growth behavior and dependence of fracture toughness on microstructural parameters such as, volume fraction, size and spacing of inclusions, and matrix material properties such as, strain hardening exponent, susceptibility to secondary void nucleation and energy dissipated in the growth of the nucleated voids, observed in experiments, naturally emerge in our calculations. The extent to which the microstructural parameters and matrix material properties affect the micromechanisms of ductile crack advance and the macroscopic fracture toughness of the material were illustrated.

The key conclusions are as follows:

1. For material microstructures consisting of a ductile matrix with three-dimensional (random) distribution of void nucleating inclusions, it is not possible to identify or distinguish between the void-by-void and the multiple-void interaction micromechanisms of ductile crack advance.
2. Our results show that there is an increase in the propensity of plastic strain localization with increasing inclusion volume fraction and/or inclusion size.
3. Due to the increase in the propensity of plastic strain localization for high inclusion volume fraction and large inclusion size, $J_{IC}/(\sigma_0 l_0)$ only depends on the inclusion size while for relatively low inclusion volume fraction and small inclusion size, $J_{IC}/(\sigma_0 l_0)$ depends on both the inclusion size and the overall microstructural parameter i.e. inclusion volume fraction.
4. The dependence of $J_{IC}/(\sigma_0 l_0)$ on the inclusion volume fraction for small inclusions decreases with decreasing strain hardening exponent of the matrix material, increasing susceptibility of secondary void nucleation and decreasing energy dissipation in the growth of nucleated voids prior to ductile crack advance.
5. The results presented provide guidelines for microstructural engineering to increase ductile fracture toughness, for example, the results show that for a material with small inclusions, increasing the mean inclusion spacing has a greater effect on fracture toughness than for a material with large inclusions.

Acknowledgments

The large-scale finite element calculations reported on were carried out using high performance research computing resources provided by Texas A&M University (http://hprc.tamu.edu). The financial support provided by the U.S. National Science Foundation grant CMMI - 1663130 (AS), and European Union's Horizon2020 Programme (Excellent Science, Marie-Sklodowska - Curie Actions, H2020 - MSCA - RISE - 2017) under REA grant agreement 777896 (Project QUANTIFY, SO and AS) are gratefully acknowledged. The authors are very grateful for the many fruitful discussions with Dr. Alan Needleman (Texas & M University, College Station, TX).

References

References

Amar, E., Pineau, A., 1985. Interpretation of ductile fracture toughness temperature dependence of a low strength steel in terms of a local approach. Engineering Fracture Mechanics 22 (6), 1061–1071.

Aravas, N., McMeeking, R. M., 1985a. Finite element analysis of void growth near a blunting crack tip. Journal of the Mechanics and Physics of Solids 33 (1), 25–49.

Aravas, N., McMeeking, R. M., 1985b. Microvoid growth and failure in the ligament between a hole and a blunt crack tip. International Journal of Fracture 29 (1), 21–38.

ASTM:E1820-11, 2011. Standard test method for measurement of fracture toughness. ASTM International.

Becker, R., 1987. The effect of porosity distribution on ductile failure. Journal of the Mechanics and Physics of Solids 35 (5), 577–599.

Belytschko, T., Chiapetta, R. L., Bartel, H. D., 1976. Efficient large scale non-linear transient analysis by finite elements. International Journal for Numerical Methods in Engineering 10 (3), 579–596.

Benzerga, A. A., Besson, J., Pineau, A., 1999. Coalescence-controlled anisotropic ductile fracture. Journal of Engineering Materials and Technology 121 (2), 221–229.

Benzerga, A. A., Leblond, J.-B., 2010. Ductile fracture by void growth to coalescence. In: Advances in applied mechanics. Vol. 44. Elsevier, pp. 169–305.

Benzerga, A. A., Leblond, J.-B., Needleman, A., Tvergaard, V., 2016. Ductile failure modeling. International Journal of Fracture 201 (1), 29–80.

Birat, J.-P., 2016. Steel cleanliness and environmental metallurgy. Metallurgical Research & Technology 113 (2), 201.

Birkle, A. J., Wei, R. P., Pellissier, G. E., 1966. Analysis of plane-strain fracture in a series of 0. 45 c-ni-cr-mo steels with different sulfur contents. ASM Trans Quart 59 (4), 981–990.

Bourcier, R. J., Koss, D. A., Smelser, R. E., Richmond, O., 1986. The influence of porosity on the deformation and fracture of alloys. Acta Metallurgica 34 (12), 2443–2453.

Chu, C. C., Needleman, A., 1980. Void nucleation effects in biaxially stretched sheets. Journal of engineering materials and technology 102 (3), 249–256.

Cox, T. B., Low, J. R., 1974. An investigation of the plastic fracture of aisi 4340 and 18 nickel-200 grade maraging steels. Metallurgical Transactions 5 (6), 1457–1470.

Dubensky, E. M., Koss, D. A., 1987. Void/pore distributions and ductile fracture. Metallurgical Transactions A 18 (11), 1887–1895.

Edelson, B. I., Baldwin Jr, W. M., 1959. The effect of second phases on the mechanical properties of alloys. Tech. rep., DTIC Document.

Gall, K., Horstemeyer, M., McDowell, D. L., Fan, J., 2000. Finite element analysis of the stress distributions near damaged si particle clusters in cast al–si alloys. Mechanics of Materials 32 (5), 277–301.

Gao, X., Faleskog, J., Shih, C. F., Dodds Jr, R. H., 1998. Ductile tearing in part-through cracks: experiments and cell-model predictions. Engineering fracture mechanics 59 (6), 761–777.

Gao, X., Wang, T., Kim, J., 2005. On ductile fracture initiation toughness: effects of void volume fraction, void shape and void distribution. International Journal of Solids and Structures 42 (18-19), 5097–5117.

Garrison, W. M., Moody, N. R., 1987. The influence of inclusion spacing and microstructure on the fracture toughness of the secondary hardening steel af1410. Metallurgical Transactions A 18 (7), 1257–1263.

Garrison, W. M., Wojcieszynski, A. L., Iorio, L. E., 1997. Effects of inclusion distributions on the fracture toughness of structural steels. Recent advances in Fracture, 361–372.

Garrison Jr, W. M., Wojcieszynski, A. L., 2009. A discussion of the spacing of inclusions in the volume and of the spacing of inclusion nucleated voids on fracture surfaces of steels. Materials Science and Engineering: A 505 (1-2), 52–61.

Ghahremaninezhad, A., Ravi-Chandar, K., 2012a. Deformation and failure in nodular cast iron. Acta Materialia 60 (5), 2359–2368.

Ghahremaninezhad, A., Ravi-Chandar, K., 2012b. Ductile failure behavior of polycrystalline al 6061-t6. International journal of fracture 174 (2), 177–202.

Goods, S. H., Brown, L. M., 1979. Overview no. 1: The nucleation of cavities by plastic deformation. Acta metallurgica 27 (1), 1–15.

Green, G., Knott, J. F., 1976. The initiation and propagation of ductile fracture in low strength steels. Journal of Engineering Materials and Technology 98 (1), 37–46.

Gurland, J., Plateau, J., 1963. The mechanism of ductile rupture of metals containing particles. Trans. ASM

56, 442–454.
Gurson, A. L., 1975. Plastic flow and fracture behavior of ductile materials incorporating void nucleation, growth and coalescence. PhD Diss, Brown University.
Hahn, G. T., Kanninen, M. F., Rosenfield, A. R., 1972. Fracture toughness of materials. Annual Review of Materials Science 2 (1), 381–404.
Hahn, G. T., Rosenfield, A. R., 1975. Metallurgical factors affecting fracture toughness of aluminum alloys. Metallurgical Transactions A 6 (4), 653–668.
Hannard, F., Simar, A., Maire, E., Pardoen, T., 2018. Quantitative assessment of the impact of second phase particle arrangement on damage and fracture anisotropy. Acta Materialia 148, 456–466.
Hom, C. L., McMeeking, R. M., 1989. Three-dimensional void growth before a blunting crack tip. Journal of the Mechanics and Physics of Solids 37 (3), 395–415.
Jie, L., Feng, G., Zhi, L., Wang, J.-L., Yan, M.-G., 2007. Influence of sizes of inclusions and voids on fracture toughness of ultra-high strength steel aermet100. Journal of Iron and Steel Research, International 14 (5), 254–258.
Kim, J., Gao, X., Srivatsan, T. S., 2003. Modeling of crack growth in ductile solids: a three-dimensional analysis. International journal of solids and structures 40 (26), 7357–7374.
Kim, J., Zhang, G., Gao, X., 2007. Modeling of ductile fracture: application of the mechanism-based concepts. International journal of solids and structures 44 (6), 1844–1862.
Krafft, J. M., 1964. Correlation of plane strain crack toughness with strain hardening characteristics of a low, a medium, and a high strength steel. Applied Materials Research 3 (2), 83–96.
Lautridou, J. C., Pineau, A., 1981. Crack initiation and stable crack growth resistance in a508 steels in relation to inclusion distribution. Engineering Fracture Mechanics 15 (1-2), 55–71.
Martin, J. W., 2012. Precipitation hardening: theory and applications. Butterworth-Heinemann.
McMeeking, R. M., 1977. Finite deformation analysis of crack-tip opening in elastic-plastic materials and implications for fracture. Journal of the Mechanics and Physics of Solids 25 (5), 357–381.
Needleman, A., Tvergaard, V., 1987. An analysis of ductile rupture modes at a crack tip. Journal of the Mechanics and Physics of Solids 35 (2), 151–183.
Osovski, S., Srivastava, A., Ponson, L., Bouchaud, E., Tvergaard, V., Ravi-Chandar, K., Needleman, A., 2015a. The effect of loading rate on ductile fracture toughness and fracture surface roughness. Journal of the Mechanics and Physics of Solids 76, 20–46.
Osovski, S., Srivastava, A., Williams, J. C., Needleman, A., 2015b. Grain boundary crack growth in metastable titanium β alloys. Acta Materialia 82, 167–178.
Pan, J., Saje, M., Needleman, A., 1983. Localization of deformation in rate sensitive porous plastic solids. International Journal of Fracture 21 (4), 261–278.
Pardoen, T., Hutchinson, J. W., 2003. Micromechanics-based model for trends in toughness of ductile metals. Acta Materialia 51 (1), 133–148.
Passoja, D. E., Hill, D. C., 1974. On the distribution of energy in the ductile fracture of high strength steels. Metallurgical Transactions 5 (8), 1851–1854.
Peirce, D., Shih, C. F., Needleman, A., 1984. A tangent modulus method for rate dependent solids. Computers & Structures 18 (5), 875–887.
Puttick, K. E., 1959. Ductile fracture in metals. Philosophical magazine 4 (44), 964–969.
Rice, J. R., 1968. A path independent integral and the approximate analysis of strain concentration by notches and cracks. Journal of applied mechanics 35 (2), 379–386.
Rice, J. R., 1976. The localization of plastic deformation. In: In: Koiter W (ed) 14th International congress theoretical and applied mechanics. North–Holland, pp. 207–220.
Rice, J. R., Johnson, M. A., 1970. The role of large crack tip geometry changes in plane strain fracture. In: Inelastic behaviour of solids. McGraw-Hill, pp. 641–672.
Rogers, H. C., 1960. The tensile fracture of ductile metals. Trans Metal. Soc. AIME 218, 498–506.
Shabrov, M. N., Needleman, A., 2002. An analysis of inclusion morphology effects on void nucleation. Modelling and Simulation in Materials Science and Engineering 10 (2), 163.
Shih, C. F., 1981. Relationships between the j-integral and the crack opening displacement for stationary

and extending cracks. Journal of the Mechanics and Physics of Solids 29 (4), 305–326.
Spitzig, W., 1969. Correlations between fractographic features and plane-strain fracture toughness in an ultrahigh-strength steel. In: Electron Microfractography. ASTM International.
Srivastava, A., Osovski, S., Needleman, A., 2017. Engineering the crack path by controlling the microstructure. Journal of the Mechanics and Physics of Solids 100, 1–20.
Srivastava, A., Ponson, L., Osovski, S., Bouchaud, E., Tvergaard, V., Needleman, A., 2014. Effect of inclusion density on ductile fracture toughness and roughness. Journal of the Mechanics and Physics of Solids 63, 62–79.
Stone, R. H. V., Cox, T. B., Low, J. R., Psioda, J. A., 1985. Microstructural aspects of fracture by dimpled rupture. International Metals Reviews 30 (1), 157–180.
Tang, S., Kopacz, A. M., Chan, S., Olson, G. B., Liu, W. K., et al., 2013. Three-dimensional ductile fracture analysis with a hybrid multiresolution approach and microtomography. Journal of the Mechanics and Physics of Solids 61 (11), 2108–2124.
Tekoğlu, C., Hutchinson, J. W., Pardoen, T., 2015. On localization and void coalescence as a precursor to ductile fracture. Phil. Trans. R. Soc. A 373 (2038), 20140121.
Tinet, H., Klöcker, H., Le Coze, J., 2004. Damage analysis during hot deformation of a resulfurised stainless steel. Acta materialia 52 (13), 3825–3842.
Tipper, C. F., 1949. The fracture of metals. Metallurgia 39 (231), 133–137.
Tvergaard, V., 1981. Influence of voids on shear band instabilities under plane strain conditions. International Journal of fracture 17 (4), 389–407.
Tvergaard, V., 1982a. Influence of void nucleation on ductile shear fracture at a free surface. Journal of the Mechanics and Physics of Solids 30 (6), 399–425.
Tvergaard, V., 1982b. On localization in ductile materials containing spherical voids. International Journal of fracture 18 (4), 237–252.
Tvergaard, V., 1989. Material failure by void growth to coalescence. In: Advances in applied Mechanics. Vol. 27. Elsevier, pp. 83–151.
Tvergaard, V., 2007. Discrete modelling of ductile crack growth by void growth to coalescence. International Journal of Fracture 148 (1), 1–12.
Tvergaard, V., Hutchinson, J. W., 2002. Two mechanisms of ductile fracture: void by void growth versus multiple void interaction. International Journal of Solids and Structures 39 (13-14), 3581–3597.
Tvergaard, V., Needleman, A., 1984. Analysis of the cup-cone fracture in a round tensile bar. Acta metallurgica 32 (1), 157–169.
Van Stone, R. H., Psioda, J. A., 1975. Discussion of “metallurgical factors affecting fracture toughness of aluminum alloys”. Metallurgical Transactions A 6, 668–670.